

Viscoplastic dambreak waves: Review of simple computational approaches and comparison with experiments

C. Ancey*, N. Andreini, G. Epely-Chauvin

School of Architecture, Civil and Environmental Engineering, École Polytechnique Fédérale de Lausanne, 1015 Lausanne, Switzerland

ARTICLE INFO

Article history:

Available online 1 April 2012

Keywords:

Dam-break problem
Herschel–Bulkley fluid
Lubrication theory
Kinematic wave approximation
Saint–Venant equations

ABSTRACT

We investigated the dam-break problem for Herschel–Bulkley fluids: a fixed volume of a viscoplastic material (a polymeric gel called Carbopol ultrez 10) was released and flowed down an inclined flume. Using Particle Image Velocimetry techniques, we measured the velocity profiles far from the sidewalls, the front position as a function of time, and the flow depth evolution at a given place. The experimental data were compared to three models of increasing complexity: the kinematic wave model, an advection diffusion model (lubrication theory), and the one-layer Saint–Venant equations. Surprisingly, the best agreement was obtained with the simplest model (kinematic wave model) even though it could not capture the details of the head profile (regarded as a shock wave, i.e., a discontinuity). Lubrication theory (the advection diffusion model) performed well from a qualitative viewpoint. Computed velocity profiles and depth evolution were in reasonably good agreement with data, but this model overestimated initial acceleration, which resulted in a systematic difference between theoretical and experimental curves of the front position over time. This shortcoming was not fixed when using a more elaborate model (Saint–Venant equations), rather it was exacerbated. The relatively modest performance of the more elaborate models was intriguing (for Newtonian liquids, the best agreement was obtained with the most sophisticated model).

© 2012 Elsevier Ltd. All rights reserved.

1. Introduction

Viscoplastic models such as the Herschel–Bulkley and Casson models have been extensively used in engineering and geophysical fluid mechanics as an idealization of materials that behave like solids when at rest, but like liquids when sufficient stress is applied [15,3]. The significance of viscoplastic models has been extensively debated from different perspectives. Their relevance to natural flows such as snow avalanches and debris flows has been questioned: while a few field observations and experiments support their relevance [24,36,22,38], there is also increasing evidence that the behavior of sediment laden flows may contrast significantly with the predictions of viscoplastic flow theory [35]. From the rheometric standpoint, there are also considerable difficulties related to the measurements of rheological properties in conventional rheometers, which arise from technological constraints (e.g., proper computation of shear rate in a wide-gap rheometer, wall slip control) [2,50] and/or occurrence of more complicated effects (e.g., viscoelasticity, thixotropy) [49]. The mere existence of a true yield stress has been a hot topic for a long time [14,17]. Controversies and debates also arose in the development of flow-dynamics models for

viscoplastic fluids, i.e. models that compute pressure-driven flows in pipes or the spreading of a fluid over a surface. A feature of viscoplastic flows is the occurrence of rigid regions (where the material does not deform under the action of applied stresses) surrounded by flow regions (where the material has yielded and deforms continuously). A key issue is then the interplay between the flowing and unsheared/stagnant regions. The occurrence of rigid regions (also referred to as *plugs*) raises a number of difficulties from the mathematical and numerical points of view. Naïve use of computational methods that perform well for Newtonian fluids leads to paradoxes. One classic example is the existence of genuinely unsheared region in nonuniform free-surface flows [52,11]: since for free-surface flows, the shear stress tends to zero approaching the free surface, it has been argued that the upper layers should be unyielding and move as a rigid block, but if the flow is nonuniform, the plug velocity should also vary in the downstream distance to accommodate flow depth changes, which conflicts with the rigidity of the upper layers. A consistent asymptotic treatment shows that the upper layers are not unyielding, but slightly sheared [11]. Regularization of viscoplastic constitutive equations in numerical models has also led to convergence problems [27]. The lessons one can learn from these investigations are that (i) it is much harder to find correct approximations of the stress field for viscoplastic materials than for Newtonian fluids and (ii) small errors in the stress

* Corresponding author.

E-mail address: christophe.ancey@epfl.ch (C. Ancey).

estimates may lead to substantial errors in the strain rate computation. In this context, glean information about the performance of simple flow-dynamics models is of paramount importance.

The objective of the present paper is to review some of the efforts to model viscoplastic flows down an inclined flume, highlight the crucial assumptions, and compare the results with a set of new data. Most current models exploit the flow shallowness to simplify the local mass and momentum balance equations (Cauchy equations) a great deal and derive governing equations that are analytically tractable or easier to solve numerically than the original conservation equations. For viscoplastic flows over horizontal or inclined surfaces, the use of a lubrication approximation dates back to Liu and Mei [43,44]. Further theoretical insights and extensions were given by Balmforth et al. [10,13,12], Matson and Hogg [46], Hogg and Matson [30], and Ancey and Cochard [5]. Lubrication models are regarded as appropriate approximations provided that the flow is sufficiently slow for inertia to have negligible effects [47]. When the inertia terms can no longer be neglected in the momentum balance equation, the governing equations are usually derived by averaging the local conservation equations over the stream depth. While the earliest models were *ad hoc* adaptations of the shallow water equations (also referred to as the *Saint-Venant equations*) [21,39,26], growing attention has been paid to derivations of the governing equations using consistent asymptotic expansions of near-equilibrium solutions to the Cauchy equations [32,25].

An outline of our paper is as follows. In Section 2, we start with a review of the main notions used hereafter, in particular the velocity profiles and shear stress distribution for uniform and slightly nonuniform flows of Herschel–Bulkley fluids. Emphasis is given to simple shear flows (we do not provide a full overview of rheological behavior and stress computation for viscoplastic materials). In Section 3, we describe the experimental facility and protocol. We also provide velocity profiles for different slopes and times. In Section 4, we outline three theoretical models in common use: the kinematic wave model, an advection diffusion model (lubrication theory), and the one-layer Saint-Venant equations. We briefly describe the governing equations and how solutions can be obtained. Note that the goal was not to develop new models or numerical solvers, but to present a fair comparison of models of increasing complexity. A failed attempt to solve the three-dimensional problem using commonly used numerical techniques (generalized Navier–Stokes solver based on a finite-difference scheme, level-set function for the free-surface, Chorin projection and implicit solver for the stress term) is presented in Rentschler's PhD thesis [54]; this relative failure underlines the difficulties encountered in the numerical simulations of three-dimensional free-surface viscoplastic flows. We end the paper with a few concluding remarks (see Section 5).

2. Fundamentals: velocity and shear stress profiles

2.1. Steady uniform flow

Let us consider a steady uniform flow of viscoplastic fluid over an inclined surface. Slope is denoted by θ . The x coordinate aligns with the streamwise direction, and the y -axis is normal to the flow direction. We focus on Herschel–Bulkley fluids, which are simple viscoplastic fluids with a well-defined yield stress τ_c . The material is incompressible, with density ρ . Independently of the constitutive equation, the shear stress distribution throughout the depth is $\tau(y) = \rho g(h - y) \sin \theta$, where h denotes the flow depth and g is the gravitational acceleration. The no-slip condition is assumed for the streamwise velocity component u at the bottom: $u(0) = 0$.

For a simple shear flow, the Herschel–Bulkley model reads

$$\tau = \tau_c + \mu \dot{\gamma}^n, \quad (1)$$

where $\dot{\gamma} = du/dy$ denotes the shear rate, μ is called consistency and n is the shear-thinning index (shear-thinning because for most materials $n < 1$) [15]. The shear stress is undefined for $\dot{\gamma} < 0$. The case $n = 1$ is called the Bingham model. The integration of the constitutive equation provides the cross-stream velocity profile

$$u(y) = \frac{nA}{n+1} \begin{cases} (Y_0^{1+1/n} - (Y_0 - y)^{1+1/n}) & \text{for } y \leq Y_0, \\ Y_0^{1+1/n} & \text{for } y \geq Y_0, \end{cases} \quad (2)$$

where

$$Y_0 = h - h_c, \quad A = \left(\frac{\rho g \sin \theta}{\mu} \right)^{1/n}, \quad \text{and } h_c = \tau_c / (\rho g \sin \theta). \quad (3)$$

We refer to h_c as the critical flow depth (no steady uniform flow is possible for $h < h_c$) and Y_0 the position of the yield surface, i.e. the interface separating the sheared ($y < Y_0$) and unyielding ($y > Y_0$) regions. A further integration leads to the depth-averaged velocity

$$\bar{u} = \frac{nA}{(n+1)(2n+1)} \frac{h(1+n) + nh_c}{h} Y_0^{1+1/n} \quad (4)$$

provided that $\tau_b > \tau_c$ (or equivalently $h > h_c$): when $\tau_b < \tau_c$, no steady uniform flow takes place. Eq. (4) allows us to derive an expression for the bottom shear stress as a function of \bar{u}/h by substituting $\rho g \sin \theta$ with τ_b/h into (4)

$$\left(\frac{\mu}{\tau_c} \right)^{1/n} \frac{2n+1}{n} \frac{\bar{u}}{h} = \left(\frac{\tau_b}{\tau_c} \right)^{1/n} \left(1 - \frac{\tau_c}{\tau_b} \right)^{1+1/n} \left(1 + \frac{n}{n+1} \frac{\tau_c}{\tau_b} \right). \quad (5)$$

This nonlinear implicit equation is seldom used in this form. Huang and Garcia [32] used the following formulation that is reminiscent of the Newtonian case

$$\tau_b = \tau_c + \mu \left(\frac{n}{n+1} \frac{u_p}{Y_0} \right)^n, \quad (6)$$

with u_p the plug velocity [$u_p = u(Y_0)$ in Eq. (2)]. Although this equation is fully consistent with Eq. (5), it involves Y_0 in its parametrization, which makes it less helpful for one-layer flow models (Y_0 is unknown for nonuniform flow conditions). Huang and Garcia [32] bypassed this difficulty by using a two-layer model to compute not only the flow depth h , but also the yield surface position Y_0 .

Closed equations for the bottom shear expression have been proposed for particular values of the shear-thinning index. For $n = 1/3$, Coussot [21] proposed the following fit

$$\tau_b = \tau_c (1 + 1.93G^{3/10}) \quad \text{with } G = \left(\frac{\mu}{\tau_c} \right)^3 \frac{\bar{u}}{h}, \quad (7)$$

which was obtained by solving Eq. (5) for a wide range of the dimensionless group G and interpolating the data with a power-law function. The relative divergence in the estimate of τ_b between Eqs. (5) and (7) is less than 2% for G in the 10^{-3} – 10^3 range. Much of the analysis has been done for $n = 1$ (Bingham model). Huang and Garcia [31] derived an exact expression for the bottom shear stress $\tau_b = \tau_c + 2\mu u_p/Y_0$ with u_p the plug velocity: $u_p = 3h\bar{u}/(3h - Y_0)$. This expression has the disadvantage of Y_0 dependence, as for the general case, which makes it of little help to simple models. Pastor et al. [51] reviewed several empirical approximations to Eq. (5) with $n = 1$, which can also be cast in the equivalent form

$$(1 - \xi^2)(2 + \xi) = a\xi, \quad (8)$$

with $\xi = \tau_c/\tau_b$ and $a = 6\mu\bar{u}/(h\tau_c)$. As the discriminant of this equation is negative, the analytical solutions produced by Cardan's formula are complex numbers, but their imaginary part cancels out (the three roots are thus real); the only physically admissible solution is the one that satisfies $0 \leq \xi \leq 1$. It can be more convenient to

use numerical approximations which are easier to compute. Pastor et al. [51] proposed the following second-order polynomial to approximate the third-order polynomial:

$$\frac{3}{2}\zeta^2 - \left(\frac{57}{16} + a\right) + \frac{65}{32} = 0. \quad (9)$$

2.2. Nonuniform flow

When the flow is slightly nonuniform, the shear stress alters as a result of the changes in the free-surface gradient. A common approach is to start from the Cauchy momentum balance equation in which the inertia terms have been neglected together with the normal stress gradient [43,47]. Here we closely follow Mei's derivation used by almost all subsequent authors [47]. With the assumption of negligible inertia, the downstream projection of the momentum balance equation reads

$$0 = \rho g \sin \theta - \frac{\partial p}{\partial x} + \frac{\partial \tau}{\partial y},$$

For slightly nonuniform flows, the pressure is found to be hydrostatic to leading order: $p = \rho g(h - y)\cos\theta$. The shear stress distribution is then

$$\tau = \rho g(h - y) \cos \theta \left(\tan \theta - \frac{\partial h}{\partial x} \right). \quad (10)$$

The integration of the constitutive Eq. (1) yields:

$$u(y) = \frac{nK}{n+1} \left(\tan \theta - \frac{\partial h}{\partial x} \right)^{1/n} \begin{cases} \left(Y_0^{1+1/n} - (Y_0 - y)^{1+1/n} \right) & \text{for } y \leq Y_0, \\ Y_0^{1+1/n} & \text{for } y \geq Y_0, \end{cases} \quad (11)$$

where we introduced the yield surface position Y_0 and parameter K

$$Y_0 = h - h_c \left(1 - \cos \theta \frac{\partial h}{\partial x} \right)^{-1} \quad \text{and} \quad K = \left(\frac{\rho g \cos \theta}{\mu} \right)^{1/n}. \quad (12)$$

The definition of the critical depth is the same: $h_c = \tau_c / (\rho g \sin \theta)$. A new integration leads to the depth-averaged velocity for nonuniform flows

$$\bar{u} = \frac{nK}{(n+1)(2n+1)} \left(\tan \theta - \frac{\partial h}{\partial x} \right)^{1/n} \frac{h(1+n) + nh_c}{h} Y_0^{1+1/n}. \quad (13)$$

The departure from the steady uniform flow is reflected through a correction factor $(1 - \cot \theta \partial_x h)^{1/n}$ and the non-constant position of the yield surface Y_0 . The correction factor can take large values because, on the one hand, $1/n$ is usually large (typically 3 or greater) and, on the other hand, the free-surface gradient $\partial_x h$ becomes significant within the head. Note also the influence of slope on the correction factor: for shallow slopes ($\theta \rightarrow 0$), the effect of the free-surface gradient is greatly amplified since $\cot \theta \rightarrow \infty$. Following a long tradition in hydraulics [20], the bottom shear stress for nonuniform flows is usually computed as if the flow were locally uniform. Although this assumption makes sense for turbulent water, it is arguable here because of the strong nonlinearities in the rheological behavior. Indeed, as stated in the introduction, small errors in the stress field computation may lead to large errors in the strain rate computation.

2.3. Sidewall effect correction

All the calculations above hold for infinitely wide flows over inclined rigid boundaries. The effect of finite width on the flow rate of viscoplastic fluids has been investigated by a few authors. Whipple [57] carried out numerical finite-element simulations to study the flow rate of Bingham fluids through rectangular, trapezoidal,

and semi-circular cross-sections. For wide sections, he found that his simulations were consistent with the shear stress predicted by Eq. (8). Coussot [21] fit a function of the same form as (7) to his experimental data (kaolin suspensions in rectangular channels) to take the flume width W into account

$$\tau_b = \tau_c (1 + aG^{3/10}) \quad \text{with } a = 1.93 - 0.43 \arctan \left[\left(10 \frac{h}{W} \right)^{20} \right]. \quad (14)$$

It is worth noting that this equation leads to a decrease in the bottom shear stress with increasing ratio h/W , which contrasts markedly with the behavior of Newtonian fluids and turbulent flows. Burger et al. [18,19] extended the Darcy–Weisbach formulation to non-Newtonian fluids, including Herschel–Bulkley fluids

$$\tau_b = \frac{1}{2} f \rho \bar{u}^2 \quad \text{with } f = \frac{K}{Re}. \quad (15)$$

They introduced a generalized Reynolds number whose expression was

$$Re = \frac{8\rho\bar{u}^2}{\tau_c + \mu \left(\frac{2\bar{u}}{R_h} \right)^n} \quad \text{with } R_h = \frac{Wh}{W + 2h}$$

for a rectangular cross-section through a Herschel–Bulkley fluid, where R_h denotes hydraulics. By studying steady uniform flows of power-law and viscoplastic flows, they found $K = 16.4$ for rectangular cross-sections. Taking a closer look at Eq. (15) in the limit $h/W \rightarrow 0$ (which should provide a solution close to that given by Eq. (6)) shows that this empirical relation holds for $n \rightarrow 1$ and $\tau_b \gg \tau_c$ (i.e., Bingham fluids with low yield stress). In conclusion, we emphasize that these earlier works barely scratched the surface of the topic. As far as we know, there is no general method for computing sidewall drag for open channel flows of viscoplastic fluid.

3. Experimental facility and procedure

3.1. Experimental facility and procedure

We used Carbopol ultrez 10 at a mass concentration of 0.15%. Given the low concentration of Carbopol, the density is that of water: $\rho = 1000 \text{ kg m}^{-3}$. All the experiments reported here were carried out with an initial volume $\mathcal{V} = 6 \text{ l}$. The sample was prepared as follows: the Carbopol powder was gently poured and dispersed in a large volume of demineralized water heated at $55 \text{ }^\circ\text{C}$. The dispersion was left to rest for a few hours (typically one night). The pH was adjusted to 7.70 ± 0.05 by adding a sodium hydroxide solution. After mixing the sample vigorously, we added a tiny amount of polyamid particles (for PIV measurements, see below). To ensure homogeneity and remove air bubbles trapped during the previous phases, we mixed the sample very slowly (4 rpm) for 12 h. We measured the rheological properties using a parallel plate geometry (with serrated plates, diameter 60 mm and gap 2 mm) mounted on a Bohlin CVOR rheometer. On average, we had: $\tau_c = 33 \text{ Pa}$, $n = 0.33$, and $\mu = 26 \text{ Pa s}^n$. Reproducibility tests carried out with other geometries showed that the uncertainty on the rheological parameters was more pronounced than for Newtonian liquids. We estimated that the maximum deviation was $\Delta\tau_c = 2 \text{ Pa}$ (relative uncertainty 6%), $\Delta n = 0.02$ (relative uncertainty 6%), and $\Delta\mu = 4 \text{ Pa s}^n$ (relative uncertainty 15%). Additional tests showed that Carbopol ultrez 10 was negligibly viscoelastic and thixotropic.

All our Carbopol samples were seeded with polyamid particles for particle imaging velocimetry. The particles (manufactured by Dantec Dynamics, mean diameter $20 \text{ }\mu\text{m}$) were marked with rhodamine by leaving them in a concentrated rhodamine solution (maintained at $60 \text{ }^\circ\text{C}$) for one month. They were then rinsed with

alcohol several times to avoid subsequent contamination of the samples by rhodamine.

Experiments were conducted in a PMMA-bottomed flume with aluminium sidewalls. Fig. 1 shows a sketch of the facility. The flume was 3.5 m long and 10 cm wide. It could be inclined from 0 deg to 35 deg. Its position was accurately controlled using a digital inclinometer with a precision of 0.1 deg. The upper part of flume was equipped with a sluice gate mounted on a pneumatic jack and was used as a reservoir. The jack was quickly raised by injecting air pressured at 7 MPa, which made it possible to lift the gate within 0.5 s. The gate was a ultrahigh molecular weight polyethylene plate that minimized friction with the suspension retained behind it. This reduced friction limited upward fluid motion when the gate was raised.

We took the following measurements: (i) the velocity profile throughout the experiment at $x = 255$ cm in a vertical plane Oxy passing through the centerline of the flume ($z = 5$ cm) and normal to the flume bottom, (ii) the position of the front as a function of time, and (iii) the flow depth evolution at $x = 255$ cm. To that end, we used a dual head, diode pumped, Q-switched Nd:YLF Laser (Litron LDY 303). The laser had two optical cavities emitting a 527-nm beam (green), with energy up to 20 mJ per pulse at 1 kHz. Velocities were measured using high-speed cameras and particle image velocimetry (PIV) techniques. For PIV measurements, we used a Basler A504k camera (working in the 200–1000 Hz range), mounted with a Nikkor 105 mm macro lens and an orange filter. The images were then processed using classic PIV techniques [53]. Velocity fields were computed using the open source software, MatPIV [56]. The front position was monitored using two Basler A403kc cameras.

Fig. 2 illustrates how we measured the velocity profiles from below using the Scheimpflug principle [see [53], chap. 7]. Filming from the side, it was not possible to measure velocities within the head far from the sidewall owing to the strong curvature (in both x - and z -axis) and flow shallowness of the front. Conversely, filming from below gave direct optical access to the vertical plane passing through the centerline, but the disadvantage of this configuration was that the largest part of the filmed plane was out of focus. To eliminate this problem, we adjusted the inclinations of the camera CCD and the lens so that the Scheimpflug rule was satisfied (the image was then in focus). A prism (made up of a PMMA block,

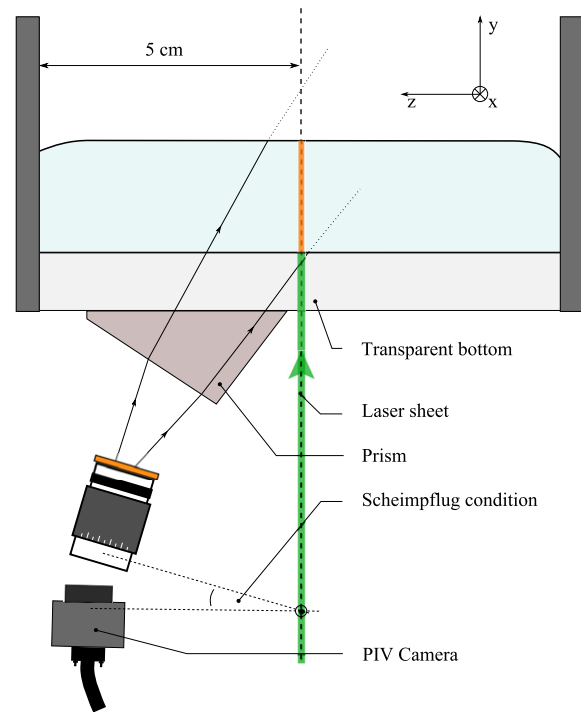


Fig. 2. Sketch of the measurement system for the velocity profiles within the moving fluid. Because of the fluid/air interface and the three-dimensional nature of the flows, we were forced to film the flow from below. In that case, the CCD sensor is no longer parallel to the filmed plane and the images are blurred. To get around this issue, one can use the Scheimpflug principle, which involves tilting the camera until the image plane (on the CCD), the lens plane, and the object plane (lit by the laser sheet) have a common line of intersection.

with the same refractive index as that of the flume bottom) was necessary to avoid refraction. As this system caused significant image distortion, we had to correct it to properly compute the velocity field; this was done by taking a shot of a test chart and using the Matlab built-in function *cp2form* to undistort the images.

3.2. Experimental velocity profiles

We start the comparison of theoretical predictions with experimental data by taking a closer look at the velocity profiles obtained with a Carbopol gel for two slopes: $\theta = 15$ deg and $\theta = 25$ deg. As the other flow variables such as the front position and flow depth profile involve further theoretical computations, they will be introduced in the next section. To provide further points of comparison and discussion, we have included an appendix that presents a few results obtained with a Newtonian fluid (98.5%-glycerol solution, viscosity $\mu = 1.11$ Pa s, and density $\rho = 1260$ kg m⁻³).

For the sake of simplicity and brevity, we have decided to present only two flume inclinations, which were representative of the flow pattern observed. For slopes shallower than 10 deg, the flow came to a halt rapidly. As shown presently, slopes $\theta = 15$ deg and $\theta = 25$ deg exhibited distinctive features even though the flows looked similar.

Fig. 3 shows the measured profiles and theoretical velocity profiles (11) for a flume inclination $\theta = 25$ deg. Each subplot corresponds to a different time, but rather than providing the time at which the velocity measurements were taken, we gave the position of the front x_f relative the point of measurement ($x = 255$ cm). When compared to the mean flow depth $h \sim 20$ mm, this relative distance $\Delta x = x - x_f$ indicates whether the flow slice that we were filming belongs to the head or the body. Note that in Fig. 3, the flow was from

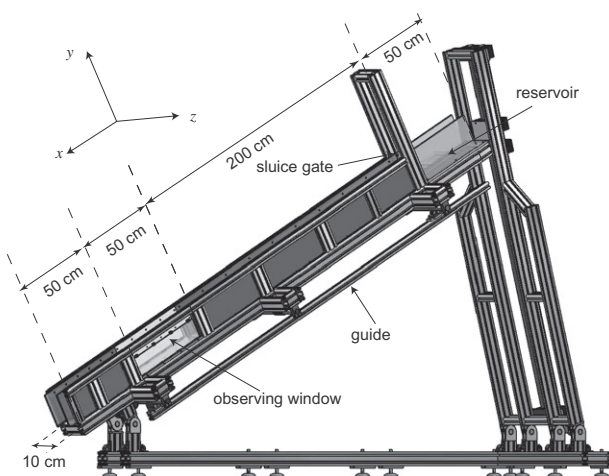


Fig. 1. Flume used for the experiments. We defined a two-dimensional Cartesian coordinate system in which the x -axis points down the flume, the y -axis is in the direction of the upward pointing normal, and the z -axis is the cross-stream direction. The upper end of the flume is at $x = 0$, while the lower end is at $x = 350$ cm. $z = 0$ refers to the right sidewall (when looking at the flume from the inlet), while $z = W = 10$ cm refers to the left sidewall.

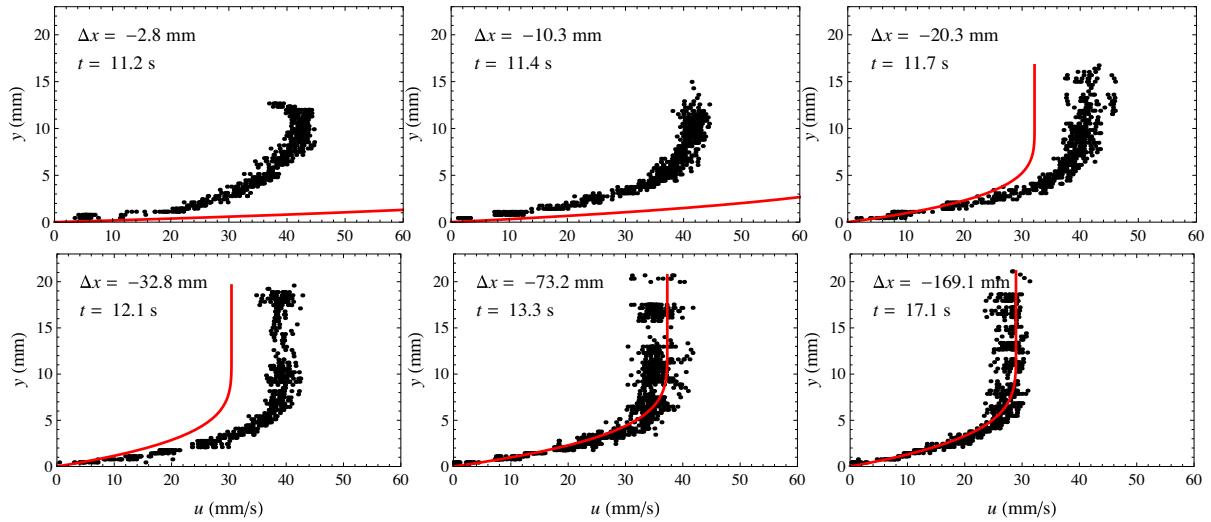


Fig. 3. Velocity profiles at $x = 255$ cm for $\theta = 25$ deg and an initial volume $V = 6.1$. Dots: experimental values; (red) curves: theoretical profiles given by Eq. (11) with $\rho = 1000$ kg m $^{-3}$, $\tau_c = 33$ Pa, $n = 0.33$, and $\mu = 26$ Pa s n . We also report the distance Δx between the front position x_f and the point of measurement $x = 255$ cm ($\Delta x < 0$ because the front is on the right of the point of measurement) together with the time at which the profile was measured. Use of Eq. (11) requires an equation specifying the gradient of the free surface $\partial_x h(x, t)$. We evaluated $\partial_x h(x, t)$ experimentally by interpolating the measured flow depths by a piecewise linear function: the slope of each segment gave a fairly good local estimate of $\partial_x h(x, t)$. (For interpretation of the references to colour in this figure legend, the reader is referred to the web version of this article.)

left to right, thus Δx was negative. As detailed below, there was clearly a difference between the velocity field within the head ($|\Delta x/h| \leq 3$) and the velocity field within the body ($|\Delta x/h| > 3$). When the front was far away from the point of measurement at $x = 255$ cm, i.e. when the distance to the front was large $\Delta x \leq -73.2$ mm, there was good agreement between the theoretical velocity profile (11) (for nonuniform flow conditions) and the experimental data. In contrast, close to the front ($\Delta x \geq -32.8$ mm), this agreement became poorer and poorer: the theoretical velocities were significantly higher than those observed. The discrepancy near the contact line was expected since the theoretical profile was derived for flow conditions slightly departed from the steady uniform regime; within the tip region, the assumption of slightly nonuniform should break down because of the curvature of the surface. Another interesting feature was the existence of a pseudo-plug far from the front whereas the leading edge was entirely sheared across the depth (see the discussion in the introduction). This was qualitatively consistent with the rapid increase in the shear stress induced by the free-surface curvature predicted by Eq. (10). From a quantitative viewpoint, however, the discrepancy between theoretical and experimental velocity profiles may indicate that the flow conditions within the head could not be described within the framework of lubrication theory and/or the rheological behavior could not be fully captured by the Herschel–Bulkley equation.

Fig. 4 shows the velocity profiles for a flume inclination $\theta = 15$ deg. At first sight, these profiles look like those pertaining to $\theta = 25$ deg, but a closer look at the profiles reveals distinctive features. First, although the velocity data were noisy, the pseudo-plug seemed to be slightly sheared, a point that was consistent with lubrication theory [11]. Second, the velocity profiles did not drop to zero at the bottom within the head, but tended to a constant value of 1.7 mm/s. Interestingly, slipping was observed at the shallowest slopes, but not at the steepest. Careful inspection of the close-up images confirmed that slip occurred for $\theta = 15$ deg, whereas it could not be observed for $\theta = 25$ deg. This may be consistent with other experimental investigations that reported an increase in the slip velocity with wall shear stress [37]: the shear stress increase in the tip region would cause slipping. However, this interpretation conflicts with experimental observations for $\theta = 25$ deg: for that inclination, no wall slip was observed,

even in the close vicinity of the neighborhood, a region of higher shear stress.

To sum up, we found that the theoretical velocity profiles were in good agreement with experimental data as long as the flow depth curvature was small. In contrast, within the head, there was partial or poor agreement between theory and experiment. A noticeable feature was the appearance of wall slip at the shallowest slopes.

4. Comparison with theoretical models

To compare theoretical and experimental velocity profiles, the knowledge of the flow depth and depth-gradient is sufficient to compute the theoretical profile (11). To go farther into the analysis of the performance of the Herschel–Bulkley model for time-dependent free-surface flows, we need to use flow-dynamics models that compute various flow variables such as the flow depth and the front position. In the following, we will investigate the dam-break problem, i.e. the flow of a fixed volume of viscoplastic fluid over an inclined surface. Three different models of increasing complexity will be addressed: (i) the kinematic wave approximation, which results in a hyperbolic nonlinear advection equation for the flow depth, (ii) the (non linear) advection diffusion equation obtained using lubrication theory, and (iii) the Saint-Venant equations, which are a set of hyperbolic partial differential equations.

We consider the following boundary initial value problem (see Fig. 5). Initially, a volume V (per unit width) of fluid is contained in a reservoir of length ℓ . The flume inclination is θ . The fluid is at rest with initial depth profile:

$$h(x, 0) = h_0(x) = h_g + (x - \ell) \tan \theta, \quad (16)$$

with h_g the depth at the lockgate, $h_g = V/\ell + \frac{1}{2}\ell \tan \theta$. If the volume is too small, the reservoir is not entirely filled. There is a condition on the fluid volume:

$$V \geq V_c = \frac{1}{2}\ell^2 \tan \theta \quad (17)$$

for the reservoir to be filled (i.e. with the upstream and downstream walls in contact with the fluid). If this condition is not satisfied, then

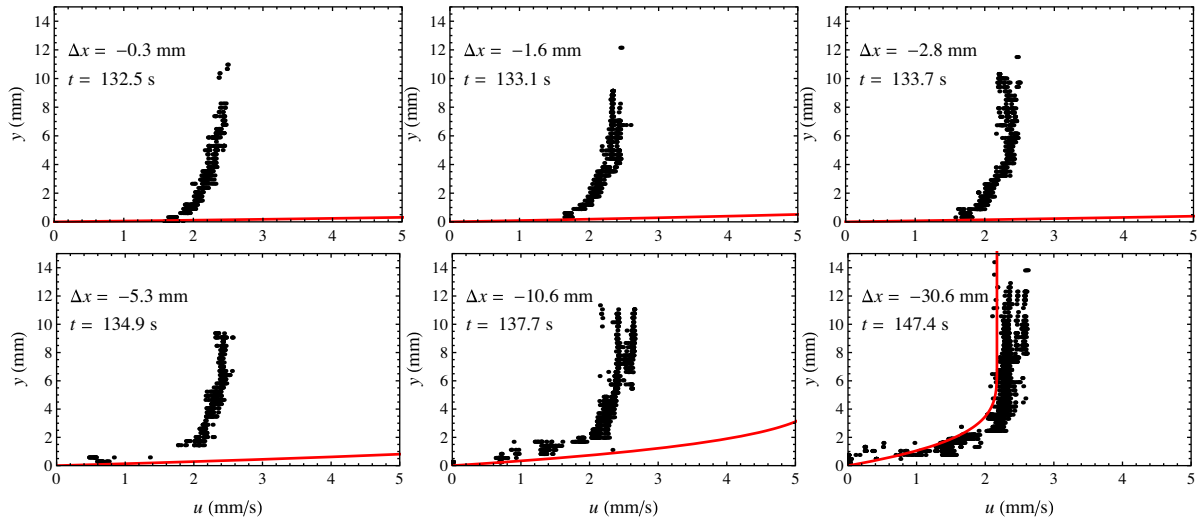


Fig. 4. Velocity profiles at $x = 255$ cm for $\theta = 15$ deg and an initial volume $\mathcal{V} = 6$ l. Dots: experimental values; (red) curves: theoretical profiles given by Eq. (11) with $\rho = 1000$ kg m $^{-3}$, $\tau_c = 33$ Pa, $n = 0.33$, and $\mu = 26$ Pa s n . Same caption as for Fig. 3. (For interpretation of the references to colour in this figure legend, the reader is referred to the web version of this article.)

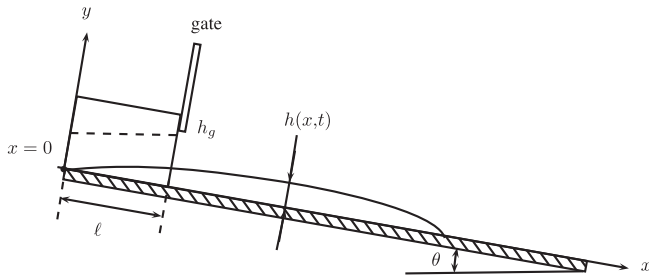


Fig. 5. Sketch defining the initial flow configuration. Initially, the fluid is at rest and the free surface (dashed line) is a straight line whose equation is given by (16). The fluid then spreads out. In the following, we are interested in computing the flow depth profile $h(x, t)$ and the front position, i.e. the point x_f at which the depth drops to zero.

the fluid wets only the downstream wall (lockgate) and fills the reservoir over a length

$$\ell_r = \sqrt{\frac{2V}{\tan \theta}}. \quad (18)$$

4.1. Kinematic wave model

The kinematic wave approximation is a common approach to describing slightly nonuniform flow for which the depth-averaged velocity adapts instantaneously to any change in the flow depth [42]. Surprisingly, the approximation is sufficiently robust to provide fairly good results for strong time-dependent flows such as dam-break waves for turbulent water flows [33] and laminar Newtonian flows [34,6]. For this reason, it has been used to model dam-break waves for Bingham and Herschel–Bulkley fluids [9,31,32].

In the framework of the kinematic wave approximation, the flow is assumed to be locally uniform. The variations in the depth-averaged velocity are then dictated by the flow depth alone: $\bar{u} = \bar{u}(h)$ is then given by Eq. (4). The bulk mass balance

$$\frac{\partial h}{\partial t} + \frac{\partial h\bar{u}}{\partial x} = 0 \quad (19)$$

provides the governing equation for h :

$$\frac{\partial h}{\partial t} + f'(h) \frac{\partial h}{\partial x} = 0, \quad (20)$$

with

$$f'(h) = Ah(h - h_c)^{1/n} \text{ and } A = \left(\frac{qg \sin \theta}{\mu} \right)^{1/n}.$$

This nonlinear advection equation can be solved easily using the method of characteristics. Eq. (20) can be put into the so-called characteristic form

$$\frac{dh}{dt} = 0 \text{ along the characteristic curve } \frac{dx}{dt} = f'(h). \quad (21)$$

These characteristic curves are straight lines whose slope is dictated by the initial depth:

$$x = f'(h_0(x_0))t + x_0, \quad (22)$$

where $h_0(x_0)$ is the initial value of h at x_0 , which is given by the initial condition (16). As $h = h_0$ along the characteristic curve, and using (16) to eliminate x_0 , we obtain an implicit equation for h :

$$x = Ah(h - h_c)^{1/n}t + (h - h_g) \cot \theta + \ell. \quad (23)$$

For the Bingham case ($n = 1$), this is a second-order polynomial that can be solved analytically [31]. For other n values, this equation has to be solved numerically.

The method of characteristics holds everywhere that the initial depth is continuous. At time $t = 0$ (and at short times), it does not work at the reservoir boundaries where the depth profile exhibits discontinuities. When the reservoir is not entirely filled (see Fig. 6), the fluid thickness drops continuously to zero: $h_0 = 0$ at $x = \ell_r$, but at the lockgate $x = \ell$ it is discontinuous. When the reservoir is filled (see Fig. 7), there are two discontinuities. A Riemann problem is associated with each discontinuity. Let us take a closer look at this double Riemann problem.

On the left (at $x = 0$), a rarefaction wave takes place. It is the similarity solution $H(\zeta)$ (with $\zeta = x/t$) to Eq. (20)

$$f'(H) = \zeta \Rightarrow Ah(h - h_c)^{1/n} = \zeta, \quad (24)$$

which does not admit analytical solutions except for $n = 1$ (Bingham fluid) and $n = 1/2$. For the Bingham case, it is straightforward to show that the flow depth is

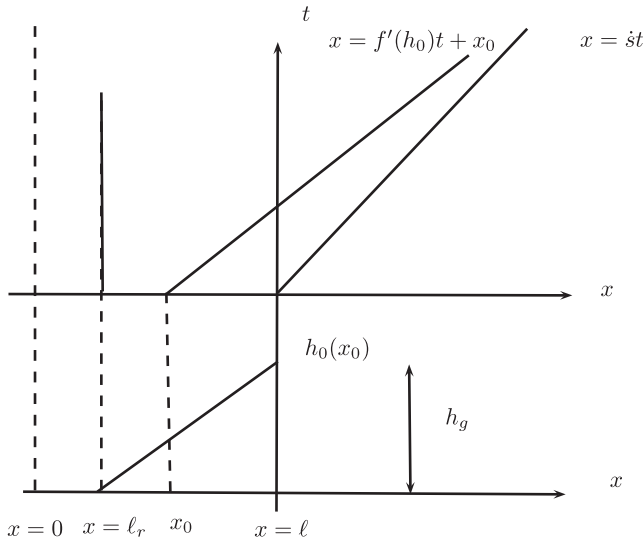


Fig. 6. Characteristic diagram when the reservoir is partially filled ($V < V_c$). Construction of the solution to the boundary initial-value problem: the solution is constant along characteristic curves, which are the one-parameter family of curves given by $\dot{x} = f'(h)$. Solving this equation on the interval $[\ell_r, \ell]$ provides the lines along which h is constant. The value of the constant along a characteristic emanating from any abscissa x_0 is given by the initial value $h_0(x_0)$. The front characteristic is a shock wave as the initial depth is discontinuous at $x = \ell$. Its equation is given by the Rankine–Hugoniot jump condition (26).

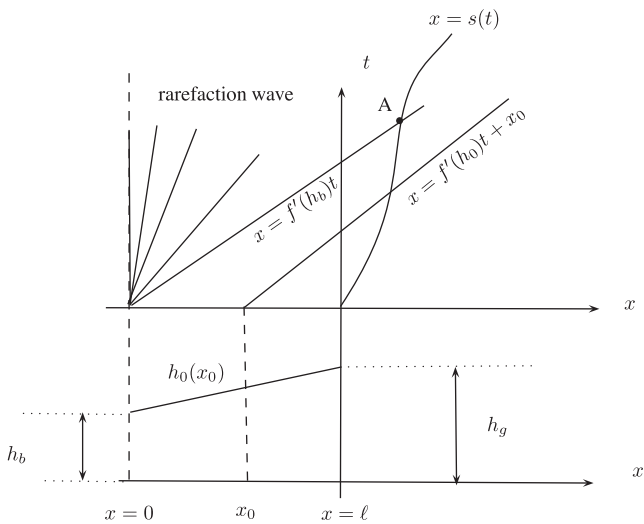


Fig. 7. Characteristic diagram when the reservoir is filled ($V \geq V_c$). Essentially, the main difference with Fig. 6 lies in the nature of the rear characteristic curve. As the solution is discontinuous at $x = 0$, we need to solve a Riemann problem. Here the solution is a centered rarefaction wave, i.e. a fan of characteristic curves emanating from the point $x = 0$. The slope of these characteristic curves ranges from 0 to $f'(h_b)$. Note also that, when solving the Rankine–Hugoniot Eq. (26), we find that the fastest characteristic curve emanating from the point $x = 0$ catches up with the front. When this occurs (at point A), the effects of the initial conditions have dissipated and the flow dynamics are controlled by the rarefaction wave.

$$h(x, t) = \sqrt{\frac{\mu}{\rho g \sin \theta} \frac{x}{t} + \left(\frac{h_c}{2}\right)^2} + \frac{1}{2} h_c. \quad (25)$$

In the characteristic diagram, this solution is represented by an expansion fan of straight lines emanating from the origin point: $x = mt$, with $0 \leq m \leq f'(h_b)$ (where $h_b = h_0(0) = h_g - \ell \tan \theta$ is the fluid thickness at the upstream end).

On the right (at $x = \ell$), there is a shock that moves along the $x = s(t)$ curve. Its features can be computed using the Rankine Hugoniot relation:

$$\dot{s} = \frac{[[f(h)]]}{[[h]]} = \frac{nA}{(n+1)(2n+1)} \frac{h_f(1+n) + nh_c}{h_f} (h_f - h_c)^{1+1/n}, \quad (26)$$

with h_f the flow depth at the front. There is no analytical solution to this equation. Its numerical resolution involves closing Eq. (26) with an equation specifying the variations in the front height h_f . Two cases have to be considered depending on what occurs behind the front:

- At short times, the details of the initial conditions influence motion and Eq. (23) holds true on the left of the shock wave. By solving the system of Eqs. (23) and (26), we obtain the equation for the front depth h_f until time t_A . This time corresponds to the intersection of the shock curve with the rarefaction wave emanating from $x = 0$ (see Fig. 7). The system of Eqs. (23) and (26) has to be solved numerically.
- At longer times ($t > t_A$), the behavior of the tail is dictated by the rarefaction wave. The governing equation for the front is then given by Eqs. (26) and (24).

A shortcoming in the kinematic wave approximation lies in the front behavior. The key assumption that underpins the derivation of the governing Eq. (20) is that for the bulk of the flow, the depth varies uniformly and slowly so that inertia and pressure gradient terms can be neglected in the momentum balance equation (the gravitational forces are then counterbalanced by the shear-stress gradient). This assumption should break down in the tip region. Indeed the flow depth drops to zero at the front and therefore, the pressure gradient can no longer be neglected in the momentum balance equation. It can be shown that a boundary layer correction at the front can fix this issue, but at the cost of more complicated calculations [5]. As this correction goes beyond the scope of the present paper, we will not use it.

Fig. 8 shows the evolution of the front position $x_f(t)$ and the time variations in the flow depth at $x_0 = 255$ cm for $\theta = 25$ deg. Both experimental and theoretical results have been reported. There was excellent agreement between theory and experiment for this slope. The main difference concerned the shape of the $h(x_0, t)$ curves: since theory predicted that the front was a shock wave while the body was a rarefaction wave, there was a sudden increase of the flow depth followed by a slow decrease. Experimentally, the passage of the front was smoother; in particular, there was no kink point at the front (this slight shortcoming can be remedied by using the boundary layer correction mentioned above). Another difference was the front behavior at short times ($t < 1$ s), but since the assumptions underpinning the kinematic wave approximation (shallow flow close to a steady uniform flow) were violated, this shortcoming could be anticipated.

Fig. 9 shows the same plots (front position $x_f(t)$ and depth evolution $h(x_0, t)$) for $\theta = 15$ deg. There was partial concordance between theory and experiments. For the front position $x_f(t)$, the experimental data revealed that, initially, the bulk accelerated less vigorously than predicted. After the slumping phase (corresponding to the first 5 s after the lockgate was removed), there was a second phase, in which the flow decelerated slowly and the changes in the front position scaled as $x_f \propto t^m$ with $m = 0.02 \pm 0.005$. This second phase was fairly well accounted for by theory since theory predicted $x_f \propto t^{0.034}$. Although these exponent values did not match, they were fairly close. In contrast, there was no agreement between the theoretical and measured evolution of flow depth $h(x_0, t)$. As for $\theta = 25$ deg, theory predicted a discontinuous evolution of the flow depth whereas experimentally, the flow depth

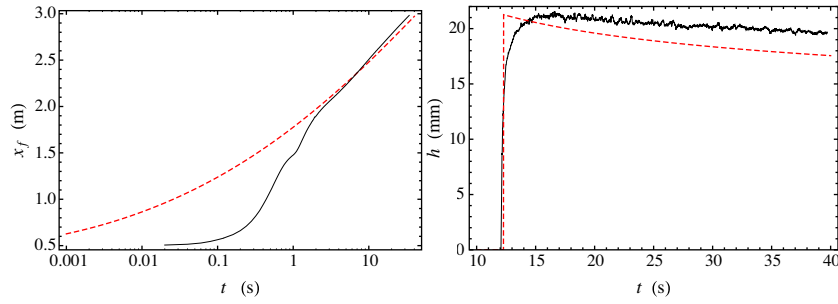


Fig. 8. Results for a slope of 25 deg and an initial volume $\nu = 6$ l. Left: Position of the front as a function of time. Right: Flow depth variation at $x_0 = 255$ cm. Experimental data: solid line. Theoretical predictions: dashed line. Note that because of the slight delay in the theoretical front velocity (with respect to the measured velocity), the time axis of the theoretical curve $h(x_0, t)$ has been slightly shifted (by $\Delta t = -1.2$ s) so that the curves $h(x_0, t)$ have the same starting point to facilitate comparison.

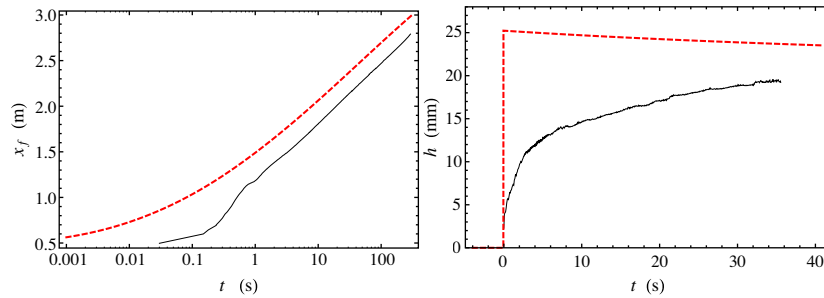


Fig. 9. Results for a slope of 15 deg and an initial volume $\nu = 6$ l. Position of the front as a function of time. Flow depth variation at $x_0 = 255$ cm. Experimental data: solid line. Theoretical predictions: dashed line. Note that because of the slight delay in the theoretical front velocity (with respect to the measured velocity), the time axis of the theoretical curve $h(x_0, t)$ has been slightly shifted (by $\Delta t = 76$ s) so that the curves $h(x_0, t)$ have the same starting point to facilitate comparison.

increased slowly and smoothly. Indeed, the shape of the leading edge was closer to a blunt nose than a shock wave. As a result, the passage of the front was not reflected by an abrupt increase in the flow depth, but by a slow growth.

4.2. Advection diffusion equation

We can elaborate on the kinematic wave model by considering that in elongating flows, the depth averaged velocity should depend on the free-surface gradient. In that case, the mean velocity is given by Eq. (13) instead of Eq. (4). Substituting the former relation into the mass conservation Eq. (19), we obtain the following governing equation for h

$$\frac{\partial h}{\partial t} + nK \frac{\partial}{\partial x} \left[\left(\tan \theta - \frac{\partial h}{\partial x} \right)^{1/n} \frac{h(1+n) + nh_c}{(n+1)(2n+1)} Y_0^{1+1/n} \right] = 0, \quad (27)$$

$$\text{with } Y_0 = \max \left(0, h - h_c \left| 1 - \cos \theta \frac{\partial h}{\partial x} \right|^{-1} \right). \quad (28)$$

As far as we are aware, this equation was first obtained by Liu and Mei [44] for Bingham fluids, then used and/or extended to Herschel–Bulkley fluids and three-dimensional problems by a number of authors including Balmforth et al. [10], Mei et al. [47], Mei and Yuhi [48], Balmforth et al. [13,12], Hogg and Matson [30], and Ancey and Cochard [5]. When the dependence on the free-surface gradient is taken into account, a diffusive term appears in the governing equation, which is likely to play a key role in regions with a marked curvature of the free surface (e.g., the head).

There is no analytical method available to solve, even approximately, this parabolic partial differential equation. There are a few solvers available, which are well-suited to computing numerical solutions to parabolic-elliptic equations in one space variable [55,16]. We used the Matlab built-in routine called *pdepe*, which is based on an algorithm developed by Skeel and Berzins [55].

Fig. 10 shows the front position over time and the evolution in the flow depth $x_0 = 255$ cm for a flume slope $\theta = 25$ deg. Surprisingly, this model, which was more complicated than the kinematic wave model seen above, provided less satisfactory results. In particular the difference between the theoretical and experimental front position was increased. Note that the long-term trend ($x_f \propto t^{0.02}$) was preserved, which shows that the deviation mainly resulted from the short-time behavior of the numerical solution. In short, the model overestimated initial acceleration.

Fig. 11 shows the front position and flow depth evolutions for a flume slope $\theta = 15$ deg. For the front position, there was not much difference in the model performance between the numerical solution to the nonlinear advection diffusion Eq. (27) and the solution to the advection Eq. (20): the refined model performed as well as the simplified kinematic wave model, but not better. In contrast, the flow depth evolution at $x_0 = 255$ cm was better captured, at least at short times after the passage of the front. This tends to show that diffusive effects are of paramount importance to the dynamics of viscoplastic flows on mild slopes and must be taken into account in theoretical models.

4.3. Depth-averaged equations

The next step in our analysis of model performance is to consider that the depth-averaged velocity is not related to the flow depth through closed-form relations such as (4) or (13), but must be computed by solving the momentum balance equation. To that end, we will use the conservative form of the Saint Venant equations

$$\frac{\partial h}{\partial t} + \frac{\partial h\bar{u}}{\partial x} = 0, \quad (29)$$

$$\frac{\partial h\bar{u}}{\partial t} + \frac{\partial h\bar{u}^2}{\partial x} + gh \cos \theta \frac{\partial h}{\partial x} = gh \sin \theta - \frac{\tau_b}{\rho}, \quad (30)$$

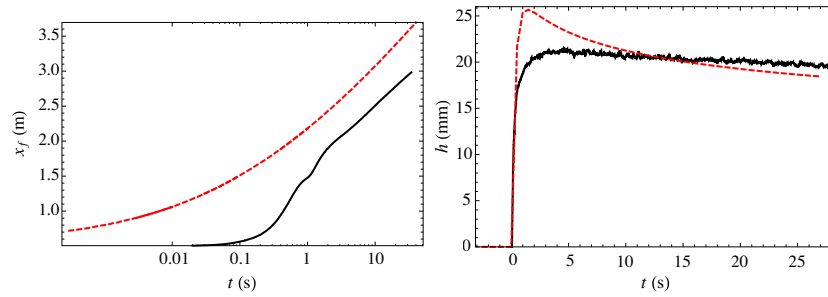


Fig. 10. Results for a slope of 25 deg and an initial volume $\mathcal{V} = 6$ l. Left: position of the front as a function of time. Right: flow depth variation at $x_0 = 255$ cm. Experimental data: solid line. Theoretical predictions: dashed line obtained by numerically solving Eq. (27). Because of the delay in the experimental front position relative to the computed front position, the time axis of the theoretical curve $h(x_0, t)$ has been shifted by $\Delta t = 94$ s so that the curves $h(x_0, t)$ have the same starting point to facilitate comparison.

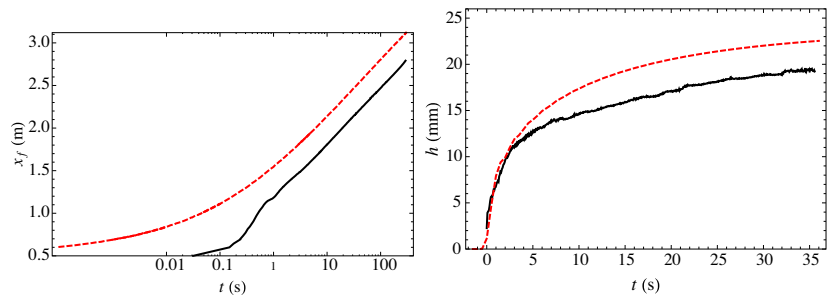


Fig. 11. Results for a slope 15 deg and an initial volume $\mathcal{V} = 6$ l. Left: position of the front as a function of time. Right: flow depth variation at $x_0 = 255$ cm. Because of the delay in the experimental front position relative to the computed front position, the time axis of the theoretical curve $h(x_0, t)$ has been shifted by $\Delta t = 84$ s. Same caption as for Fig. 10.

where $\tau_b(u, h)$ is the bottom shear stress, which can be computed using Eq. (7), since for our Carbopol samples, the shear-thinning index is very close to $n = 1/3$. These equations have been used by a number of authors including Martinet [45], Coussot [21], Laigle and Coussot [39], Fraccarollo and Papa [26], and Debiane [23] (the reader is referred to [1,3,4] for a review of these computational models for snow avalanches and mudflows). Refinements were made by Huang and García [32], who split the momentum balance equation into two parts to compute the yield surface position Y_0 in addition to the depth-averaged velocity and flow depth. This form, which is very close to the shallow water equations (except for the dissipation term), was questioned by a few authors. Piau [52] suggested supplementing the source term to account for some of the specificities of viscoplastic behavior, but additional assumptions/empirical equations were required to close the governing equations. More recently, Fernández-Nieto et al. [25] revisited the derivation of the depth-averaged equation for Bingham fluids. Starting from small perturbations to the steady solutions (to the local momentum equations), they ended up with a set of partial differential equations, which are—by the authors' own admission—very complicated to handle. For the sake of simplicity, here we will use the 'simple' depth-averaged model (29) and (30).

Eqs. (29) and (30) are hyperbolic differential equations that call for special numerical methods. We used a high-resolution wave-propagation algorithm developed by LeVeque [41]. This algorithm is a Godunov-type scheme that employs the solution to local Riemann problems. It is part of an open-source library called CLAWPACK. More specifically, we used an approximate Riemann solver developed by George [29], which provides a well-balanced scheme that preserves balanced steady states, properly captures shock waves and fronts over dry surfaces, and maintains depth non-negativity. The source term in the momentum balance equation includes two contributions: the gravitational acceleration forces (also referred to as the topography source term) and a dissipation term. The augmented Riemann solver developed by George [28,29]

incorporates topography into the momentum flux on the left-hand side of Eq. (30). The remaining source term is then the dissipative contribution τ_b/ρ . We used a fractional-step approach, with a backwards Euler scheme, to deal with this source term, as recommended by LeVeque [41]. The numerical model was successfully tested against analytical solutions to the dam break problem for inviscid fluids [7]. Comparison with similarity solutions to the viscous dam break problem also shows that this model performs well with Newtonian fluids (see Appendix A for a comparison with real fluids).

As previously, we have plotted the front position and depth evolution at $x_0 = 255$ cm for $\theta = 25$ deg (see Fig. 12) and $\theta = 15$ deg (see Fig. 13). A striking feature is the lack of concordance with experimental data. For both slopes, the numerical model overestimated the front position and contrary to the advection diffusion model, the theoretical $x_f(t)$ curve was not parallel to the experimental curve at long times, which means that the model failed to find the pseudo-equilibrium regime reached by the flow. Strikingly, the kinematic wave model, which can be seen as a simplification of the Saint-Venant equations when the assumption of near-equilibrium flow is made, was able to provide the correct trend for $x_f(t)$ at any time. The one-layer Saint-Venant model was also unable to provide accurate predictions for the depth evolution (even though the order of magnitude was correct).

The only success of the Saint-Venant model lies in the behavior of the numerical solution at short times ($t < 1$ s). For both slopes, the theoretical $x_f(t)$ curve paralleled the experimental curve whereas for the other models, initial velocities were substantially overestimated. Surprisingly, after the slumping phase, the model predicted that the front kept accelerating whereas experimentally, it reached a near-equilibrium regime characterized (as seen earlier) by a power-law behavior: $x_f(t) \propto t^m$ (with $m \sim 0.2$).

As we suspected that the overestimation of the front position was due to an improper account of sidewall effects, we carried

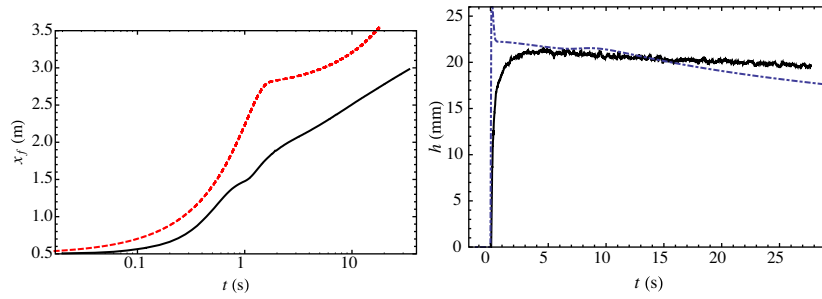


Fig. 12. Results for a slope $\theta = 25$ deg. Left: position of the front as a function of time. Right: Flow depth variation at $x = 255$ cm. Because of the delay in the experimental front position relative to the computed front position, the time axis of the theoretical curve $h(x_0, t)$ has been shifted by $\Delta t = 10.5$ s.

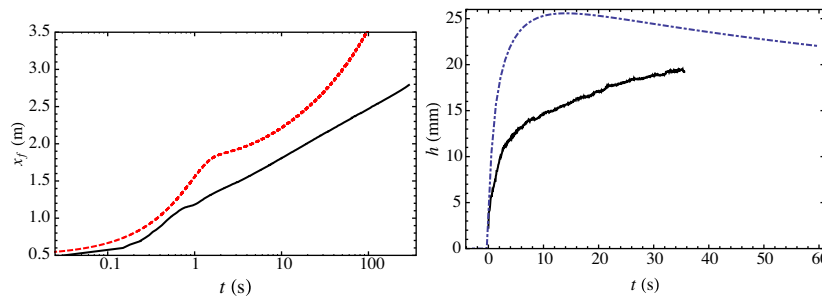


Fig. 13. Results for a slope $\theta = 15$ deg. Left: position of the front as a function of time. Right: flow depth variation at $x = 255$ cm. Because of the delay in the experimental front position relative to the computed front position, the time axis of the theoretical curve $h(x_0, t)$ has been shifted by $\Delta t = 111$ s.

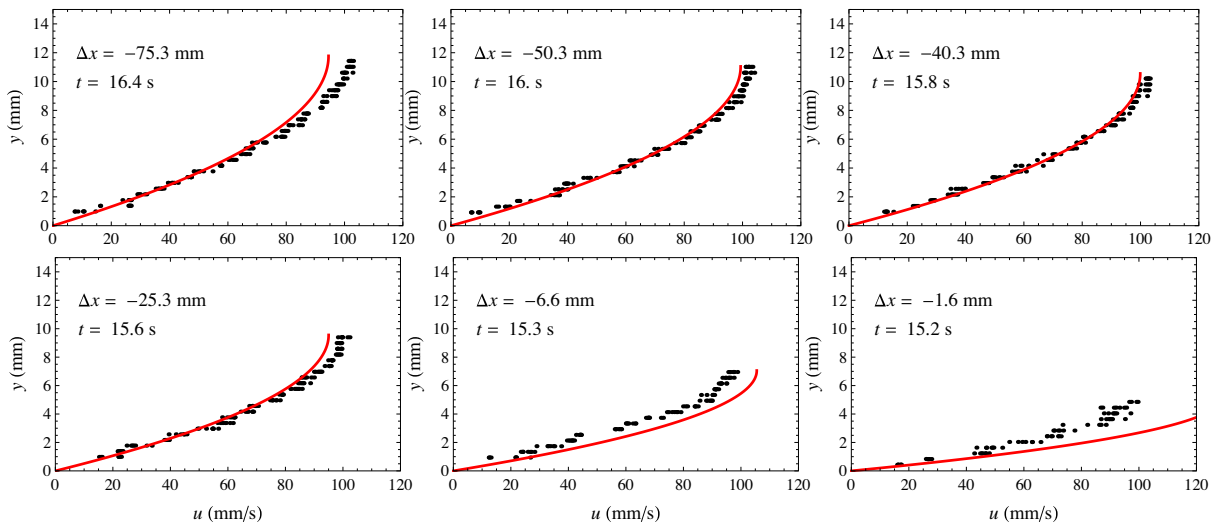


Fig. A.14. Velocity profiles at $x_0 = 255$ cm. Dots: experimental values; (red) curves: theoretical profiles given by Eq. (11) with $\rho = 1260$ kg m $^{-3}$, $\tau_c = 0$ Pa, $n = 1$, and $\mu = 1.1$ Pa s. We also report the distance Δx between the front position x_f and the point of measurement $x_0 = 255$ cm together with the time at which the data were recorded. (For interpretation of the references to colour in this figure legend, the reader is referred to the web version of this article.)

out additional simulations, in which the bottom shear stress was given by Eq. (14) or (15). Taking sidewall drag into account successfully reduced the discrepancy between experimental and computed front positions. As the empirical relations (14) and (15) could not be regarded as sufficiently accurate (see Section 2.3), it was difficult to be conclusive and properly interpret this lack of improvement after taking sidewall effects into account in the numerical simulations.

5. Concluding remarks

In this paper, we investigated the dam-break problem for Herschel–Bulkley fluids down a sloping bed. We ran experiments with

Carbopol ultrez 10, a polymeric gel whose behavior in simple shear flow is properly described using a Herschel–Bulkley model. The rheological parameters were obtained independently with a rheometer. In our experimental campaign, we measured the front position as a function of time, as well as the flow depth profile and the velocity field at a fixed position ($x_0 = 255$ cm from the flume inlet).

These benchmark experiments were designed to test and compare numerical models developed to compute the spreading of viscoplastic materials over inclined surfaces. We used three models of increasing complexity, which shared the same framework (assumption of shallow flows): the kinematic wave model, an advection diffusion model (lubrication theory), and the one-layer

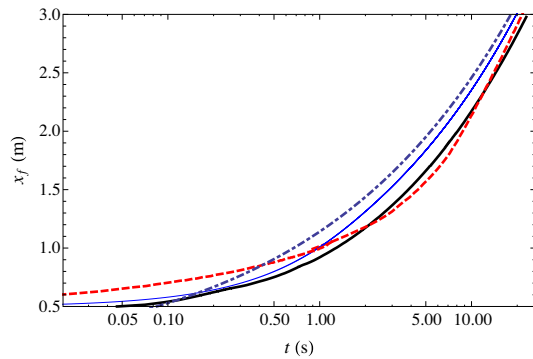


Fig. A.15. Front position with time for a 98.5% glycerol solution (density $\rho = 1260 \text{ kg m}^{-3}$, viscosity $\mu = 1110 \text{ mPa s}$ at a temperature of 20°C). Initial mass: 3 kg; flume inclination: $\theta = 6$ deg. Experimental data: thick solid line (black). Kinematic wave approximation: thin solid line (blue). Advection diffusion equation: dashed line (red). Saint-Venant equations: dot and dash line (blue). (For interpretation of the references to colour in this figure legend, the reader is referred to the web version of this article.)

Saint-Venant equations. Except for the first model (for which implicit analytical solutions were derived), the governing equations had to be solved numerically. For the advection diffusion model, we used a commercial solver (a Matlab built-in routine called *pdepe*); tests conducted with other methods (e.g., the Adams Moulton implicit scheme) did not provide significantly different results. For the Saint-Venant equations, we used the open-source library *CLAWPACK*, which provides finite-volume methods to solve hyperbolic partial differential equations [41]. More specifically, we utilized the approximate Riemann solver developed by George [28,29].¹ Each model was successfully tested against analytical solutions for flow configurations close to the problem at hand. The three models were also used to compute the spreading of a Newtonian fluid (98.5% glycerol solution) down a flume inclined at 6 deg (see Appendix A).

Surprisingly enough, there have not been many experimental investigations into the viscoplastic dam-break problem. Not only are data scarce, but also the experimental protocol was insufficiently described for careful comparison with numerical models. As far as we are aware, this paper provides the first set of high-resolution data related to the dam-break problem for Herschel–Bulkley fluids. This unique dataset is interesting in that it sheds light on unanticipated features such as wall slip (observed solely for the shallowest slopes) and the relatively poor performance of the models tested.

Strikingly, the best agreement with data was obtained with the simplest model: the kinematic wave model, which consists of a nonlinear advection equation. This model performed well for predicting the front position at steep slopes, but as, the front was merely a shock wave, it was slightly less efficient for predicting the depth evolution in the tip region; at longer times, the model gave satisfactory predictions of depth evolution. In an earlier paper [5], in which experimental data obtained with more concentrated Carbopol gels and a wider flume (30 cm instead of 10 cm) were presented, we came to similar conclusions about the good performance of the kinematic wave model at steep slopes.

In contrast, the results provided by the Saint-Venant equations were in poor concordance with experimental data. This was quite astonishing since, firstly, the kinematic wave model results from a simplification of the Saint-Venant equations and, secondly, this

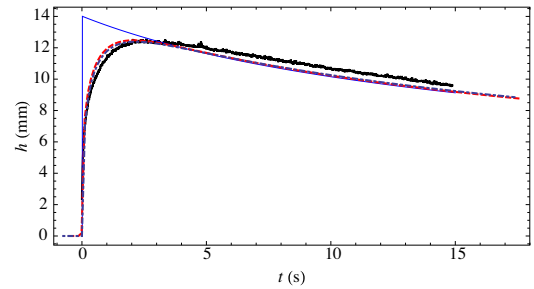


Fig. A.16. Flow depth evolution at $x_0 = 255$ cm. Experimental data: thick solid line (black). Kinematic wave model: thin solid line (blue). Advection diffusion equation: dashed line (red). Saint-Venant equations: dot and dash line (blue). Because of the delay in the theoretical front position (with respect to the measured position), the time axis for the theoretical curve $h(x_0, t)$ has been slightly shifted so that the curves $h(x_0, t)$ have the same starting point to facilitate comparison: time increment $\Delta t = 2.9$ s for the kinematic wave model, $\Delta t = 0.7$ s for the advection diffusion model, and $\Delta t = 4.2$ s for the Saint-Venant model. (For interpretation of the references to colour in this figure legend, the reader is referred to the web version of this article.)

model is of greater complexity and generality. Taking a closer look at the front position curves reveals that the Saint-Venant equations significantly overestimated velocities at short times ($t < 2$ s), i.e. just after the slumping phase. This overestimation might not seem so surprising since, for nonlinear rheologies, the Saint-Venant equations (see [40] for an example with the collapse of a granular column) are known to run into difficulty for the following reasons: (i) the assumption of a small aspect ratio (thin flow) breaks down at short times, (ii) when a mass collapses, part of the momentum is directed downwards whereas in the derivation of the Saint-Venant equations, it is assumed that the momentum flux is predominantly in the streamwise direction, (iii) for the initial stages of the flow, the assumption of simple shear flow is not realistic and thus (iv) simplified expressions such as the bottom shear stress (7) are unlikely to be of sufficient generality for computing energy dissipation in strongly nonuniform flows. Although these limitations provide explanation of the model failure at the shortest times, they do not explain why (i) the results provided by the Saint-Venant equations were much poorer than those yielded by the other models and (ii) why the model predictions were in good agreement with experimental data for Newtonian fluids (see Appendix A). Note also that taking sidewall friction into account did not change the model performance, but because of the limitations of the available empirical relations for computing sidewall drag, it was difficult to be conclusive on this.

The acknowledgement of the Herschel–Bulkley constitutive equation in the one-layer Saint-Venant equations (29) and (30) is questionable. For instance, the expression for the bottom shear stress (7) amounts to treating the material as a power-law liquid since nothing is said about the approach to the arrested state² (what happens when the shear stress drops below the yield stress?). Should we use a two-layer formulation of the Saint-Venant equations as Huang and García [32] did? Does the failure of Eqs. (29) and (30) call for a more complicated expression of the governing equations as Piau [52] and Fernández-Nieto et al. [25] suggested? The numerical method is also debatable. In the fractional-step method that we used for solving the hyperbolic problem with source term (29) and (30), the idea is to split the governing equation into two subproblems that can be solved independently: first, one solves

¹ Albeit more sophisticated, the numerical method we used for solving the Saint-Venant equations did not differ too much from other Godunov-type techniques used by Laigle and Coussot [39] and Fraccarollo and Papa [26].

² We ran numerical tests in which we considered different behaviors depending on the value of the bottom shear stress compared to the yield stress or other related values (e.g. the use of a biviscous model to regularize the constitutive equation). This did not change the front behavior, but naturally influenced the shape of the flow tail. For the sake of brevity, these additional runs have not been reported here.

the homogeneous equation (i.e., (30) with no source term), then one computes the correction imposed by the source term. This technique is known to perform well even for equations with stiff source terms, but there are also a large number of pathological cases for which the fractional-step approach fails [see Ref. [41], Chapter 17]. Note that in addition to the backward Euler scheme, we used different splitting methods to solve the second subproblem, but this did not change the outcome to any significant degree.

To us, the failure of the Saint-Venant equations in the present context comes from the oversimplified expression used for computing the bottom shear stress, rather than from flaws in the numerical methods (although these could be optimized to cope with specificities introduced by viscoplastic materials such as deposits). Testing the performance of more complete governing equations is another path to explore.

Acknowledgments

We are grateful for the financial support provided by the Swiss National Science Foundation under Grant No. 206021-133831, the competence center in Mobile Information and Communication Systems (a center supported by the Swiss National Science Foundation under Grant No. 206021_133831, MICS project), and the competence center in Environmental Sciences (TRAMM project). The third author of this paper, Gaël Epey-Chauvin, died accidentally during the writing of this paper, just before the revised version was submitted. We thank Belinda Bates for her careful reading and editing.

Appendix A. Newtonian case

To better understand the specific behavior of Carbopol and see how models perform for simple fluids, it is interesting to have a point of comparison. Here we provide additional experimental results obtained with a 98.5% glycerol solution (density $\rho = 1260 \text{ kg m}^{-3}$, viscosity $\mu = 1110 \text{ mPa s}$ at a temperature of $20 \text{ }^\circ\text{C}$). We present a single set of data; more data are available in [8]. The experimental facility and protocol were the same as those described in Section 3.1. The run presented here corresponds to a mass of 3 kg (the initial volume \mathcal{V} is 2.38 l) and a flume inclination $\theta = 6 \text{ deg}$. The flow Reynolds number was 1.13. Fig. A.14 shows the velocity profiles measured at $x_0 = 255 \text{ cm}$ for different times. The theoretical profiles are reported; they have been computed using Eq. (11) with $\mu = 1110 \text{ mPa s}$, $n = 1$, $\tau_c = 0$ (then $Y_0 = 0$). On the whole, there was excellent agreement between theoretical and experimental velocity profiles except for in the close vicinity of the contact line. For $\Delta x \geq -2.8 \text{ mm}$, theory overestimated velocity significantly. Within the tip region, there was no slip and the fluid was fully sheared.

Fig. A.15 shows the evolution of the front position with time. On the whole, all models provided fairly good predictions. For $t \geq 1 \text{ s}$, the maximum error was 9% for the kinematic wave model, 8% for the advection diffusion model, and 16% for the Saint-Venant model. The deviation from the experimental curve was larger for the Saint-Venant model than for the advection diffusion model, but the long-time trend shown by the Saint-Venant model was parallel to the experimental curve and for this reason, it could be considered to be in closer agreement with data than the advection diffusion model, which slightly overestimated the front velocity for long times.

Fig. A.16 shows the time evolution of the flow depth at $x_0 = 255 \text{ cm}$. The shape of the $h(x_0, t)$ curve predicted by the advection diffusion and Saint-Venant models was in excellent agreement with data at short times, but at long times, concordance was slightly lower: the experimental and numerical curves were parallel, but numerical simulations underestimated the flow depth by

approximately 4 to 5% (this represented a mismatch of 0.5 mm). Since the kinematic wave model regarded the leading edge as a shock wave, it failed to predict the correct shape of the depth evolution during the passage of the leading edge, but at longer times, it yielded values that closely matched those obtained using the advection diffusion and Saint-Venant models.

References

- [1] Ancey C. Snow avalanches. In: Balmforth NJ, Provenzale A, editors. Selected topics in geological and geomorphological fluid mechanics. Berlin: Springer; 2001. p. 319–38.
- [2] Ancey C. Solving the Couette inverse problem by using a wavelet-vaguelette decomposition. *J Rheol* 2005;49:441–60.
- [3] Ancey C. Plasticity and geophysical flows: a review. *J Non-Newton Fluid Mech* 2007;142:4–35.
- [4] Ancey C. Gravity flow on steep slope. In: Chassignet E, Cenedese C, editors. Buoyancy driven flows. New York: Cambridge University Press; 2012.
- [5] Ancey C, Cochard S. The dam-break problem for Herschel–Bulkley fluids down steep flumes. *J Non-Newton Fluid Mech* 2009;158:18–35.
- [6] Ancey C, Cochard S, Andreini N. The dam-break problem for viscous fluids in the high-capillary-number limit. *J Fluid Mech* 2009;624:1–22.
- [7] Ancey C, Iverson RM, Rentschler M, Denlinger RP. An exact solution for ideal dam-break floods on steep slopes. *Water Resour Res* 2008;44:W01430.
- [8] Andreini N, Epey-Chauvin G, Ancey C. Internal dynamics of Newtonian and viscoplastic fluid avalanches down a sloping bed. *Phys Fluids*; submitted for publication.
- [9] Arattano M, Savage WZ. Modelling of debris flows as kinematic waves. *Bull Int Assoc Eng Geol* 1994;49:3–13.
- [10] Balmforth NJ, Burbridge AS, Craster RV. Viscoplastic models of isothermal lava domes. *J Fluid Mech* 2000;403:37–65.
- [11] Balmforth NJ, Craster RV. A consistent thin-layer theory for Bingham plastics. *J Non-Newton Fluid Mech* 1999;84:65–81.
- [12] Balmforth NJ, Craster RV, Rust AC, Sassi R. Viscoplastic flow over an inclined surface. *J Non-Newton Fluid Mech* 2007;142:219–43.
- [13] Balmforth NJ, Craster RV, Sassi R. Shallow viscoplastic flow on an inclined plane. *J Fluid Mech* 2002;470:1–29.
- [14] Barnes HA. The yield stress – a review or ‘ $\pi\alpha\nu\tau\alpha\rho\epsilon\iota$ ’ – everything flows? *J. Non-Newton Fluid Mech* 1999;81:213–7.
- [15] Bird RB, Dai GC, Yarusso BJ. The rheology and flow of viscoplastic materials. *Rev Chem Eng* 1983;1:1–70.
- [16] Blom JG, Zegeling PA. Algorithm 731: a moving-grid interface for systems of one-dimensional time-dependent partial differential equations. *ACM Trans Math Softw* 1994;20:194–214.
- [17] Bonn D, Denn MM. Yield stress fluids slowly yield to analysis. *Science* 2009;324:1401–2.
- [18] Burger J, Haldenwang R, Alderman N. Experimental database for non-Newtonian flow in four channel shapes. *J Hydraul Res* 2010;48:363–70.
- [19] Burger J, Haldenwang R, Alderman N. Friction factor-Reynolds number relationship for laminar flow of non-Newtonian fluids in open channels of different cross-sectional shapes. *Chem Eng Sci* 2010;65:3549–56.
- [20] Chow VT, editor. Open-channel hydraulics. Civil engineering series. New York: Mc Graw Hill; 1959.
- [21] Coussot P. Mudflow rheology and dynamics. Rotterdam: Balkema; 1997.
- [22] Coussot P, Proust S, Ancey C. Rheological interpretation of deposits of yield stress fluids. *J Non-Newton Fluid Mech* 1996;66:55–70.
- [23] Debiane K. 2000. *Hydraulique des écoulements laminaires à surface libre dans un canal pour des milieux visqueux ou viscoplastiques: régimes uniformes, graduellement varié, et rupture de barrage*. Ph.D. thesis, Joseph Fourier University [in French].
- [24] Dent JD, Lang TE. Experiments on the mechanics of flowing snow. *Cold Reg Sci Technol* 1982;5:243–8.
- [25] Fernández-Nieto ED, Noble P, Vila JP. Shallow water equation for non-Newtonian fluids. *J Non-Newton Fluid Mech* 2010;165:712–32.
- [26] Fraccarollo L, Papa M. Numerical simulation of real debris-flow events. *Phys Chem Earth B* 2000;25:757–63.
- [27] Frigaard IA, Nouar C. On the usage of viscosity regularization methods for visco-plastic fluid flow computation. *J Non-Newton Fluid Mech* 2005;127:1–26.
- [28] George DL. Finite volume methods and adaptive refinement for tsunami propagation and inundation. Ph.D. thesis, University of Washington; 2006.
- [29] George DL. Augmented Riemann solvers for the shallow water equations over variable topography with steady states and inundation. *J Comput Phys* 2008;227:3089–113.
- [30] Hogg AJ, Matson GP. Slumps of viscoplastic fluids on slopes. *J Non-Newton Fluid Mech* 2009;158:101–12.
- [31] Huang X, Garcia MH. A perturbation solution for Bingham-plastic mudflows. *J Hydraul Eng* 1997;123:986–94.
- [32] Huang X, Garcia MH. A Herschel–Bulkley model for mud flow down a slope. *J Fluid Mech* 1998;374:305–33.
- [33] Hunt B. Dam-break solution. *J Hydraul Eng* 1984;110:675–86.
- [34] Hunt B. Newtonian fluid mechanics treatment of debris flows and avalanches. *J Hydraul Eng* 1994;120:1350–63.

- [35] Iverson RM. The physics of debris flows. *Rev Geophys* 1997;35:245–96.
- [36] Johnson AM, Rodine JR. Debris flow. In: Brunnsden D, Prior DB, editors. *Slope instability*. Chichester: John Wiley & Sons; 1984. p. 257–362.
- [37] Kalyon DM. Apparent slip and viscoplasticity of concentrated suspensions. *J Rheol* 2005;49(6):21–640.
- [38] Kern MA, Tiefenbacher F, McElwaine JN. The rheology of snow in large chute flows. *Cold Reg Sci Technol* 2004;39:181–92.
- [39] Laigle D, Coussot P. Numerical modeling of mudflows. *J Hydraul Eng* 1997;123:617–23.
- [40] Larrieu E, Staron L, Hinch EJ. Raining into shallow water as a description of the collapse of a column of grains. *J Fluid Mech* 2006;554:259–70.
- [41] LeVeque RJ. *Finite volume methods for hyperbolic problems*. Cambridge: Cambridge University Press; 2002.
- [42] Lighthill MJ, Whitham GB. On kinematic waves. I. Flood movement in long rivers. *Proc R Soc London Ser A* 1955;229:281–316.
- [43] Liu KF, Mei CC. Approximate equations for the slow spreading of a thin sheet of Bingham plastic fluid. *Phys Fluids A* 1990;2:30–6.
- [44] Liu KF, Mei CC. Slow spreading of a sheet of Bingham fluid on an inclined plane. *J Fluid Mech* 1990;207:505–29.
- [45] Martinet G. Contribution à la modélisation numérique des avalanches de neige dense et aux laves torrentielles. Ph.D. thesis, University Joseph Fourier; 1992 [in French].
- [46] Matson GP, Hogg AJ. Two-dimensional dam break flows of Herschel–Bulkley fluids: the approach to the arrested state. *J Non-Newton Fluid Mech* 2007;142:79–94.
- [47] Mei CC, Liu KF, Yuhi M. Mud flows – Slow and fast. In: Balmforth NJ, Provenzale A, editors. *Geomorphological fluid mechanics: selected topics in geological and geomorphological fluid mechanics*. Berlin: Springer; 2001. p. 548–77.
- [48] Mei CC, Yuhi M. Slow flow of a Bingham fluid in a shallow channel of finite width. *J Fluid Mech* 2001;431:135–59.
- [49] Møller PCF, Mewis J, Bonn D. Yield stress and thixotropy: on the difficulty of measuring yield stresses in practice. *Soft Matter* 2006;2:274–83.
- [50] Ovarlez G, Mahaut F, Bertrand F, Chateau X. Flows and heterogeneities with a vane tool: Magnetic resonance imaging measurements. *J Rheol* 2011;55:197–223.
- [51] Pastor M, Quecedo M, González E, Herreros MI, Fernández JA, Mira P. Simple approximation to bottom friction for Bingham fluid depth integrated models. *J Hydraul Eng* 2004;130:149–55.
- [52] Piau JM. Flow of a yield stress fluid in a long domain. Application to flow on an inclined plane. *J Rheol* 1996;40:711–23.
- [53] Raffel M, Willert CE, Wereley ST, Kompenhans J. *Particle image velocimetry*. Berlin: Springer; 2007.
- [54] Rentschler M. Simulating viscoplastic avalanches. Ph.D. thesis, École Polytechnique Fédérale de Lausanne; 2010.
- [55] Skeel RD, Berzins M. A method for the spatial discretization of parabolic equations in one space variable. *SIAM J Sci Stat Comput* 1990;11:1–32.
- [56] Sveen JK. An introduction to MatPIV. Technical report, Department of Mathematics, University of Oslo; 2004.
- [57] Whipple KX. Open-channel flow of Bingham fluids: application in debris-flow research. *J Geol* 1997;105:243–62.